

# Scattering by nanoplasmonic mesoscale assemblies

MD. IMRAN KHAN,<sup>1,\*</sup>, SAYANTANI GHOSH<sup>1</sup>, AND ARNOLD D. KIM,<sup>2</sup>

*Department of Physics<sup>1</sup> and Applied Mathematics<sup>2</sup>, University of California, Merced, 5200 North Lake Road, Merced, CA 95343, USA*

*\*mkhan39@ucmerced.edu*

**Abstract:** The flexibility and versatility of nanoassembled plasmonic structures provide platforms for mesoscale tunable optical modulation. Our recently developed model for these nanoassembled plasmonic structures is composed of a dielectric spherical core surrounded by a concentric spherical shell containing a random distribution of AuNPs. This model provides a useful platform for studying the role of a controlled amount of disorder on scattering by a particle. In that context, we explore the angular distribution of scattered light for different sizes (5 - 20 nm) and filling fractions (0.1 - 0.3) of the AuNP in the coatings. The simulations reveal that the coating of AuNPs redistributes power in a way that suppresses angular side lobes, thereby guiding the scattered power preferentially in the forward direction. These results highlight that with the ability to tune both the spatial and the spectral aspects of the scattering profile, these coated structures may serve as a platform for a variety of applications, including passive cloaking, scattering enhancement, and high-resolution imaging.

## 1. Introduction

Because they exhibit localized surface plasmonic coupling [1–5], metal nanoparticles have been used to control the properties of electromagnetic waves, opening opportunities for photonics applications [6–9]. Some of the unique functionalities include materials with extraordinary transmission, optical magnetism, and photonic lensing [10–16]. As in all cases of nanoassembly, these meta-structures can be constructed using either top-down or bottom-up methods. Bottom-up methods offer greater flexibility in terms of composition and morphology, while also providing a route to generate large-scale structures, extending from the nano-scale to the mesoscale and beyond [17–19]. Colloidal synthesis techniques, such as directed assembly modulated with polymer templates, DNA-mediated, or liquid crystals, are some of the few methods that have produced meta-structures composed of metal nanoparticles that have demonstrated tailored permittivity, photoconductivity, local surface plasmonic tuning, and passive cloaking through scattering suppression [17, 18, 20–24].

The authors have introduced a model for nano-assembled plasmonic metastructures consisting of a dielectric spherical core surrounded by concentric spherical shell of randomly distributed metal nanoparticles [25]. Rather than resorting to using effective medium theory or anomalous diffraction theory to model the interaction between the core and shell which have inherent scale limitations [17, 20, 26, 27], this model explicitly incorporates multiple interactions between individual metal nanoparticles in the shell and the core, allowing for core sizes comparable to the wavelength of incident light. Consequently, this model provides valuable insight into the optical properties of these metastructures across a broad range of spatial and spectral scales. We have used this model to investigate how key design parameters (nanoparticle size, filling fraction in the shell, etc.) affected the extinction properties of nano-assembled plasmonic metastructures [25]. More specifically, we have shown that this model exhibits a wide variety of complex behaviors between enhancement and suppression of scattering when core sizes are comparable to the wavelength [25], which is precisely a scale not accurately modeled using effective medium theory.

The model couples scattering by a dielectric core with the multiple scattering by the ensemble of individual metal nanoparticles that are randomly distributed in the shell. In doing so, this

model provides a theoretical framework for investigating how a controlled amount of disorder introduced by the metal nanoparticles affects the scattering by a particle. Even though aspects of this problem are physically intuitive, this model provides a systematic and quantitative method to explore fundamental mechanisms in these problems which, in turn, may lead to valuable insights for photonics applications. Our objective here is to go beyond just extinction properties and evaluate the elementary scattering properties of nanoassembled plasmonic metastructures to identify how the introduction of disordered metal nanoparticles affects scattering. Consider the classical Mie scattering problem in which a monochromatic plane wave is incident on a dielectric sphere [28]. The amplitude and phase of the field scattered by the sphere is the result of refraction and diffraction due to the boundary surface and interior material of the sphere [29]. Mathematically, the Mie solution is computed by interchanging between a cartesian coordinate system natural for the incident field to a spherical coordinate system natural for the scattered field. The cumulative result leads to complex behavior of the scattered field, especially when the sphere is comparable to the wavelength of the incident field. We typically expect that the monochromatic field scattered by a dielectric sphere whose size is comparable to the wavelength to exhibit a primary forward scattering peak, a secondary backscattering peak, and oscillatory lobes in other directions. Now consider a nano-assembled plasmonic meta structure consisting of

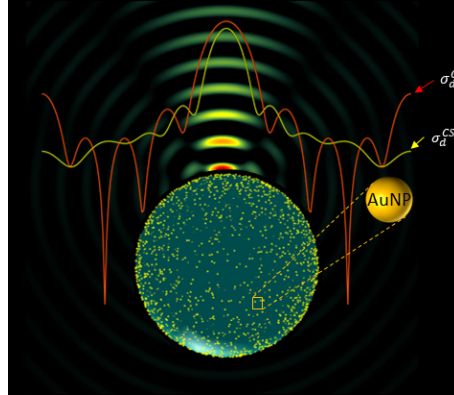


Fig. 1. The core-shell structure represented by a blue sphere (core) coated with plasmonic AuNPs (shell). The red pattern shows the differential scattering cross-section of the uncoated dielectric sphere ( $\sigma_d^C$ ), while the yellow pattern represents the same dielectric core coated with AuNPs ( $\sigma_d^{CS}$ ). The differential scattering cross-section of a plasmonic composite structure demonstrates a suppressed central lobe and smoother angular side lobes compared to the corresponding bare dielectric sphere for any particular incident wavelength.

a spherical dielectric core surrounded by a concentric shell containing a disordered ensemble of gold nanoparticles (AuNPs) as shown in Fig. 1. Each AuNP absorbs and scatters depending on its size and material composition. The ensemble of AuNPs in the shell will act as a perturbation of Mie scattering by the dielectric spherical core. The overall strength of that perturbation will depend strongly on the scattering properties of the AuNPs and their filling fraction in the shell. Multiple scattering by the AuNPs will strongly perturb the phase of the scattered field by the core because the disorder introduces a decoherence mechanism that interferes with the aforementioned refraction and diffraction by the dielectric sphere. Although we have seen that the cumulative effect of the shell of AuNPs can drastically alter the extinction of the core, we seek to understand more details about the scattering properties of these meta structures. The remainder of this paper is as follows. In Section 2 we review the features and details of the computational model. In Section 3 we review the theory of scattering by a particle and how to compute the elementary

cross-sections from the results of the computational model. We give our computational results in Section 4 that identify the key changes in behavior of scattering due to the ensemble of metal nanoparticles in the shell. Section 5 contains our conclusions.

## 2. The model

To model scattering by a spherical core surrounded by a concentric shell of randomly distributed AuNPs, we consider several fields: the interior field inside the core, denoted by  $\psi^{\text{int}}$ , the field scattered by the core, denoted by  $\psi^{\text{core}}$ , and the field scattered by each of the  $N$  AuNPs, denoted by  $\Psi_n^{\text{NP}}$  for  $n = 1, \dots, N$ . We describe our method for computing each of these fields below.

### 2.1. Interior and exterior fields

Let the core be a sphere of radius  $a$  centered at the origin of our coordinate system so that  $|\mathbf{r}| < a$  corresponds to its interior,  $|\mathbf{r}| > a$  corresponds to its exterior, and  $|\mathbf{r}| = a$  corresponds to its boundary surface. The wavenumber interior to the core is  $k_1$  and exterior to the core is  $k_0$ .

We use the method of fundamental solutions (MFS) to compute  $\psi^{\text{int}}$  and  $\psi^{\text{core}}$ . To do so, let  $\hat{\mathbf{s}}_m$  for  $m = 1, \dots, M$  denote  $M$  points that sample the unit sphere so  $|\hat{\mathbf{s}}_m| = 1$  for  $m = 1, \dots, M$ . We introduce a length  $\ell \ll a$  and write

$$\psi^{\text{int}}(\mathbf{r}) \approx \sum_{m=1}^M \frac{e^{ik_1(\mathbf{r}-(a+\ell)\hat{\mathbf{s}}_m)}}{4\pi(\mathbf{r}-(a+\ell)\hat{\mathbf{s}}_m)} c_m, \quad |\mathbf{r}| < a, \quad (1)$$

This expression gives  $\psi^{\text{int}}$  as a superposition of Green's functions. The expansion coefficients  $c_m$  for  $m = 1, \dots, M$  are to be determined. Since  $|(a+\ell)\hat{\mathbf{s}}_m| > a$  for  $m = 1, \dots, M$ , all the source points lie in the exterior. Therefore, the evaluation of (1) is an *exact* solution of

$$(\nabla^2 + k_1^2)\psi^{\text{int}} = 0, \quad |\mathbf{r}| < a. \quad (2)$$

Similarly, we write

$$\psi^{\text{core}}(\mathbf{r}) \approx \sum_{m=1}^M \frac{e^{ik_0(\mathbf{r}-(a-\ell)\hat{\mathbf{s}}_m)}}{4\pi(\mathbf{r}-(a-\ell)\hat{\mathbf{s}}_m)} b_m, \quad |\mathbf{r}| > a. \quad (3)$$

Here, the expansion coefficients  $b_m$  for  $m = 1, \dots, M$  are to be determined. In (3) the source points all satisfy  $|(a-\ell)\hat{\mathbf{s}}_m| < a$  for  $m = 1, \dots, M$ , so they all lie in the interior. Consequently, this superposition of Green's functions *exactly* satisfies

$$(\nabla^2 + k_0^2)\psi^{\text{int}} = 0, \quad |\mathbf{r}| > a. \quad (4)$$

Moreover, each Green's function satisfies the correct radiation condition for  $|\mathbf{r}| \rightarrow \infty$ , so (3) ensures that that  $\psi^{\text{core}}$  is appropriately outgoing.

### 2.2. Scattered fields by gold nanoparticles

Assuming that the AuNPs are small compared to the wavelengths in the visible spectrum, we model them as isotropic point scatterers:

$$\Psi_n^{\text{NP}}(\mathbf{r}) = \alpha_n \frac{e^{ik_0|\mathbf{r}-\mathbf{r}_n|}}{4\pi|\mathbf{r}-\mathbf{r}_n|} \psi_n^E, \quad n = 1, \dots, N, \quad (5)$$

with  $\mathbf{r}_n$  denoting the center position of the  $n$ th gold nanoparticle,  $\alpha_n$  denoting its scattering amplitude, and  $\psi_n^E$  denoting the exciting field. Let  $\sigma_s$  and  $\sigma_t$  denote scattering and total cross-sections for an individual AuNP. The scattering amplitude  $\alpha_n$  is given by [25]

$$\alpha = \left[ \frac{\sigma_s}{4\pi} - \left( \frac{k_0\sigma_t}{4\pi} \right)^2 \right]^{1/2} + i \frac{k_0\sigma_t}{4\pi}. \quad (6)$$

### 2.3. Boundary conditions

We determine the expansion coefficients,  $b_m$  and  $c_m$  for  $m = 1, \dots, M$ , and exciting fields  $\psi_n^E$  for  $n = 1, \dots, N$  using a collocation method for boundary conditions on the surface of the sphere that we explain below. The field scattered by the nanoplasmonic mesoscale assembly is

$$\psi^{\text{sca}} = \psi^{\text{core}} + \sum_{n=1}^N \Psi_n^{\text{NP}}. \quad (7)$$

We relate  $\psi^{\text{sca}}$  with  $\psi^{\text{int}}$  and the incident field  $\psi^{\text{inc}}$  through the following conditions on the boundary of the core:

$$\psi^{\text{inc}} + \psi^{\text{sca}} = \psi^{\text{int}} \quad \text{and} \quad \partial_n \psi^{\text{inc}} + \partial_n \psi^{\text{sca}} = \partial_n \psi^{\text{int}} \quad \text{on } |\mathbf{r}| = a. \quad (8)$$

Note that different boundary conditions can be specified here without any additional difficulty in implementation.

For this collocation method, we require that the conditions in (8) are satisfied on each of the points  $\mathbf{r}_m^{\text{bdy}} = a\hat{\mathbf{s}}_m$  for  $m = 1, \dots, M$ . Substituting (3) and (5) into (7) and substituting that result along with (1) into the first condition in (8) evaluated at these boundary points yields,

$$\begin{aligned} \psi^{\text{inc}}(a\hat{\mathbf{s}}_m) + \sum_{m'=1}^M G_0(|a\hat{\mathbf{s}}_m - (a - \ell)\hat{\mathbf{s}}_{m'}|)b_{m'} + \sum_{n=1}^N \alpha_n G_0(|a\hat{\mathbf{s}}_m - \mathbf{r}_n|)\psi_n^E \\ = \sum_{m'=1}^M G_1(|a\hat{\mathbf{s}}_m - (a + \ell)\hat{\mathbf{s}}_{m'}|)c_{m'}, \quad m = 1, \dots, M, \end{aligned} \quad (9)$$

with  $G_0(R) = e^{ik_0R}/(4\pi R)$  and  $G_1(R) = e^{ik_1R}/(4\pi R)$ . Performing the same procedure for the second condition in (8) and using  $\partial_n = \partial_r$  for a sphere, we obtain

$$\begin{aligned} \partial_r \psi^{\text{inc}}(a\hat{\mathbf{s}}_m) + \sum_{m'=1}^M \partial_r G_0(|a\hat{\mathbf{s}}_m - (a - \ell)\hat{\mathbf{s}}_{m'}|)b_{m'} + \sum_{n=1}^N \alpha_n \partial_r G_0(|a\hat{\mathbf{s}}_m - \mathbf{r}_n|)\psi_n^E \\ = \sum_{m'=1}^M \partial_r G_1(|a\hat{\mathbf{s}}_m - (a + \ell)\hat{\mathbf{s}}_{m'}|)c_{m'}, \quad m = 1, \dots, M. \end{aligned} \quad (10)$$

### 2.4. Exciting fields

To determine the exciting fields  $\psi_n^E$  for  $n = 1, \dots, N$ , we use the self-consistent Foldy-Lax theory [30, 31]. Consider the  $n$ th AuNP. The exciting field  $\psi_n^E$  is given by the fields scattered by the core and all *other* AuNPs. Using our approximations, this definition of the exciting fields yields

$$\psi_n^E = \sum_{m=1}^M G_0(|\mathbf{r}_n - (a - \ell)\hat{\mathbf{s}}_m|)b_m + \sum_{\substack{n'=1 \\ n' \neq n}}^N \alpha_{n'} G_0(|\mathbf{r}_n - \mathbf{r}_{n'}|)\psi_{n'}^E, \quad n = 1, \dots, N. \quad (11)$$

### 2.5. Block system

Equations (9), (10), and (11) give  $2M + N$  equations for the  $2M$  expansion coefficients  $b_m$  and  $c_m$  for  $m = 1, \dots, M$ , and  $N$  exciting fields  $\psi_n^E$  for  $n = 1, \dots, N$ . Let  $\mathbf{b} = (b_1, \dots, b_M)$ ,  $\mathbf{c} = (c_1, \dots, c_M)$  and  $\boldsymbol{\psi}^E = (\psi_1^E, \dots, \psi_N^E)$ . Equations (9), (10), and (11) can be combined

leading to the following block system:

$$\begin{pmatrix} A_1 & A_2 & B_1 \\ A_3 & A_4 & B_2 \\ & C & D \end{pmatrix} \begin{pmatrix} \mathbf{b} \\ \mathbf{c} \\ \boldsymbol{\psi}^E \end{pmatrix} = \begin{pmatrix} \mathbf{f} \\ \mathbf{g} \\ 0 \end{pmatrix}. \quad (12)$$

Here, the  $M \times M$  blocks  $A_1$ ,  $A_2$ ,  $A_3$  and  $A_4$  have entries

$$\begin{aligned} [A_1]_{m,m'} &= -G_0(|a\hat{\mathbf{s}}_m - (a - \ell)\hat{\mathbf{s}}_{m'}|), \\ [A_2]_{m,m'} &= G_1(|a\hat{\mathbf{s}}_m - (a + \ell)\hat{\mathbf{s}}_{m'}|), \\ [A_3]_{m,m'} &= -\partial_r G_0(|a\hat{\mathbf{s}}_m - (a - \ell)\hat{\mathbf{s}}_{m'}|), \\ [A_4]_{m,m'} &= \partial_r G_1(|a\hat{\mathbf{s}}_m - (a + \ell)\hat{\mathbf{s}}_{m'}|). \end{aligned}$$

The  $M \times N$  blocks  $B_1$  and  $B_2$  have entries

$$\begin{aligned} [B_1]_{m,n} &= -G_0(|a\hat{\mathbf{s}}_m - \mathbf{r}_n|)\alpha_n, \\ [B_2]_{m,n} &= -\partial_r G_0(|a\hat{\mathbf{s}}_m - \mathbf{r}_n|)\alpha_n. \end{aligned}$$

The  $N \times M$  block  $C$  has entries

$$[C]_{n,m} = -G_0(|\mathbf{r}_n - (a - \ell)\hat{\mathbf{s}}_m|),$$

and the  $N \times N$  block  $D$  has entries

$$[D]_{n,n'} = \begin{cases} 1 & n = n', \\ -G_0(|\mathbf{r}_n - \mathbf{r}_{n'}|)\alpha_{n'} & n \neq n'. \end{cases}$$

The block vectors  $\mathbf{f}$  and  $\mathbf{g}$  have entries

$$\begin{aligned} [\mathbf{f}]_m &= \psi^{\text{inc}}(a\hat{\mathbf{s}}_m), \\ [\mathbf{g}]_m &= \partial_r \psi^{\text{inc}}(a\hat{\mathbf{s}}_m). \end{aligned}$$

Upon solution of (12), we can compute  $\psi^{\text{int}}$  through evaluation of (1),  $\psi^{\text{core}}$  through evaluation of (3), and  $\Psi_n^{\text{NP}}$  through evaluation of equation (5). With  $\psi^{\text{core}}$  and  $\Psi_n^{\text{NP}}$  for  $n = 1, \dots, N$  determined, we can evaluate (7) and study its properties which we discuss below.

### 3. Scattering properties

Suppose the incident field is a plane wave with unit amplitude propagating in direction  $\hat{i}$ ,  $\psi^{\text{inc}}(\mathbf{r}) = e^{ik_0\hat{i}\cdot\mathbf{r}}$ . Using that incident field in (12), we compute the far-field behavior of  $\psi^{\text{sca}}$  given in (7) by making use of the asymptotic behavior of Green's function,

$$G_0(|R\hat{\mathbf{o}} - \mathbf{r}'|) \sim e^{-ik_0\hat{\mathbf{o}}\cdot\mathbf{r}'} \frac{e^{ik_0R}}{4\pi R}, \quad R \gg 1. \quad (13)$$

When we replace  $G_0$  by this far-field asymptotic behavior in (7), we obtain

$$\psi^{\text{sca}}(R\hat{\mathbf{o}}) \sim \left[ \frac{1}{4\pi} \sum_{m=1}^M e^{-ik_0(a-\ell)\hat{\mathbf{o}}\cdot\hat{\mathbf{s}}_m} b_m(\hat{i}) + \frac{1}{4\pi} \sum_{n=1}^N \alpha_n e^{-ik_0\hat{\mathbf{o}}\cdot\mathbf{r}_n} \psi_n^E(\hat{i}) \right] \frac{e^{ik_0R}}{R}, \quad R \gg 1. \quad (14)$$

Note that we have added the explicit dependence on the incident direction  $\hat{i}$  in the expression above. We call

$$f(\hat{\delta}, \hat{i}) = \frac{1}{4\pi} \sum_{m=1}^M e^{-ik_0(a-\ell)\hat{\delta} \cdot \hat{s}_m} b_m(\hat{i}) + \frac{1}{4\pi} \sum_{n=1}^N \alpha_n e^{-ik_0\hat{\delta} \cdot \mathbf{r}_n} \psi_n^E(\hat{i}), \quad (15)$$

the scattering amplitude for the nanoplasmonic mesoscale assembly. It gives the amplitude and phase of the scattered field in the far-field in direction  $\hat{\delta}$  due to an incident plane wave in direction  $\hat{i}$ .

We use this scattering amplitude to compute cross-sections that are used in studying scattering by particles [28,29]. First, to characterize the distribution of power scattered by the nanoplasmonic mesoscale assembly, we compute the differential scattering cross-section,

$$\sigma_d(\hat{\delta}, \hat{i}) = |f(\hat{\delta}, \hat{i})|^2. \quad (16)$$

Using the Optical Theorem, we compute the total cross-section (extinction) according to

$$\sigma_t = \frac{4\pi}{k_0} \text{Im}\{f(\hat{i}, \hat{i})\}. \quad (17)$$

The scattering cross-section is defined as

$$\sigma_s = \int_{4\pi} \sigma_d(\hat{\delta}, \hat{i}) d\hat{\delta}. \quad (18)$$

Using these cross-section, we introduce two non-dimensional parameters used to characterize scattering. The scattering albedo  $\varpi_0$  is given as

$$\varpi_0 = \sigma_s / \sigma_t, \quad (19)$$

and gives the fractional amount of  $\sigma_t$  due to  $\sigma_s$ . When  $\varpi_0 = 1$ , extinction is due entirely to scattering and when  $\varpi_0 = 0$  it is due entirely to absorption. The anisotropy factor  $g$  is defined as

$$g = \frac{1}{\sigma_t} \int_{4\pi} (\hat{\delta} \cdot \hat{i}) \sigma_d(\hat{\delta}, \hat{i}) d\hat{\delta}. \quad (20)$$

The anisotropy factor gives a measure for the amount of power flow in forward/backward directions. When  $g = 0$  scattering is isotropic and when  $g = \pm 1$  scattering is purely in the forward or backward directions, respectively.

#### 4. Results

For the following results, we have set relative refractive index for the spherical core to be  $n_r = 1.4$  corresponding to silica. We varied the core diameter from 450 nm to 750 nm, and considered the AuNPs' diameter to be either 5 nm, 10 nm, or 20 nm. AuNPs have ligands associated with them for surface functionalization [25] and we have set the ligand length to 0.98 nm. The AuNPs in the shell are distributed randomly and the minimum distance between AuNPs and the silica core is 0.98 nm since the ligand that maintains the structure and surface functionalization of AuNPs also sustains this separation distance. We use the optical properties of the AuNPs from experiments conducted on plasmonic film developed for plasmonic and nanophotonic applications by Yakubovsky *et al* [32]. The number  $N$  of the AuNPs that we used depends on the filling fraction ( $f$ ) in each case as we have explained in [25]. To compute  $\sigma_s$  and  $g$ , we used the product Gauss quadrature rule [33] with  $M = 512$  quadrature points.

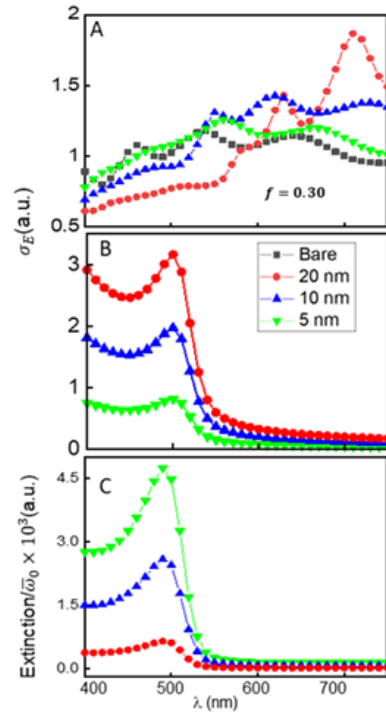


Fig. 2. (A)  $\sigma_E$  of a 750 nm bare silica sphere (black square) compared with the plasmonic core-shell structures comprised of the same core diameter but coated with varied AuNP diameters. The filling fraction was 0.30 for all AuNP sizes. A 20 nm (red dots) shell shows scattering suppression ( $\sigma_E^{CS} < \sigma_E^S$ ) from 400 nm to 600 nm of the visible spectrum. A 10 nm (blue triangle) and 5 nm (green, inverted triangle) core-shell are barely able to suppress scattering ( $\sigma_E^{CS} \approx \sigma_E^C$ ) from 400 nm to 550 nm of the visible spectrum. All core-shell structures show scattering enhancement ( $\sigma_E^{CS} > \sigma_E^C$ ) beyond 600 nm wavelength. (B) Extinction cross-section (scattering plus absorption) of a single AuNP over the visible spectrum. AuNP diameters varied as 5 nm, 10 nm, and 20 nm. (C) Ratio of extinction to their respective albedo. This ratio indicates absorption contributes more to the extinction as the AuNP size decreases.

We compute and plot the scattering efficiency, defined according to

$$\sigma_E = \frac{\sigma_t(\lambda)}{\sigma_g}$$

as function of core diameter  $d$  with  $\sigma_g$  denoting the geometric cross-section. Figure 2(A), shows the scattering efficiency for a dielectric core  $\sigma_E^C$  and a dielectric core surrounded by a plasmonic AuNP shell  $\sigma_E^{CS}$ . For the silica core,  $\sigma_g = \pi R_c^2$  with  $R_c = d/2$  denoting the radius of the core, and  $\sigma_g = \pi R_s^2$  for the core-shell assembly with  $R_s$  denoting the shell outer radius.

In Fig. 2A,  $\sigma_E^C$  exhibits oscillatory behavior characteristic of the Mie theory [28]. The peaks of those oscillations correspond to the so-called Mie resonances. The locations and heights of these peaks are characteristic of the size and relative refractive index of the sphere. In the case of plasmonic core-shell assemblies, the diameter of the core is constant at 750 nm, but the AuNPs of the shell are either 5 nm (green inverted triangle), 10 nm (blue triangle) or 20 nm (red circle). For all of these cases, the AuNP filling fraction in the shell is held constant at  $f = 0.30$ . We observe that a shell with 20 nm AuNPs suppresses scattering ( $\sigma_E^{CS} < \sigma_E^C$ ) from 400 nm to 600 nm of the visible spectrum. Here the core-shell composite shows little to no trace of Mie resonances associated with the silica core. On the other hand, the shell with 5 nm AuNPs barely suppresses scattering and closely follows  $\sigma_E^C$ . The shell with 10 nm AuNPs has a slightly higher ability to suppress scattering compared to the 5 nm AuNPs but is considerably lower than the 20 nm AuNPs.

Figure 2B shows  $\sigma_E$  for individual AuNPs. Note that the efficiencies for all three AuNP sizes exhibit an exponential decay as  $\lambda$  increases. Because of this property, we find that at these larger wavelengths, the shell of AuNPs yields enhanced scattering efficiencies ( $\sigma_E^{CS} > \sigma_E^C$ ) shown in Fig. 2A. The shell with 20 nm AuNPs has the highest extinction, especially for  $\lambda > 600$  nm, compared with 5 nm AuNPs and 10 nm AuNPs.

Figure 2C shows the total extinction ( $\sigma_E = \text{scattering} + \text{absorption}$ ) of single AuNP normalized by the respective scattering albedo ( $\bar{\omega}_0$ ). The extinction ( $\sigma_E$ ) normalized by the scattering albedo ( $\bar{\omega}_0$ ) reveals that much of the power is extinguished by the shell with 20 nm AuNPs due to scattering. In contrast, in the case of a shell with 5 nm AuNPs, power is extinguished due to absorption.

These results highlight the main mechanism of this model – the scattering spectra by the plasmonic core-shell assembly is modified (scattering suppression and enhancement) due to the strong multiple scattering by AuNPs in the shell and with the dielectric core. In the rest of the simulation, we show results of core-shell assemblies, where the shell comprises 20 nm and 5 nm AuNPs at a constant filling fraction of  $f = 0.30$ . This specific choice of AuNP diameters and filling fraction compares results between a weakly interacting plasmonic shell (5nm AuNP) and a strongly interacting shell (20 nm AuNP) at a high filling fraction ( $f = 0.30$ ).

The effective magnitude of suppression and enhancement of scattering can be altered by varying the diameter of the dielectric core while maintaining a constant size of AuNP (20 nm) and the filling fraction ( $f = 0.30$ ) in the shell. Figure 3 shows a map of  $\Delta\sigma_E = \sigma_E^{CS} - \sigma_E^C$  over the visible spectrum for various sizes of plasmonic core-shell assemblies. The variations in the dielectric core diameter, ranging from 450 nm to 750 nm. A 750 nm core-shell assembly shows scattering suppression up to 600 nm of the visible spectrum, enhancing scattering from 600 nm to 750 nm.

The assemblies of the 650 and 550 nm core-shell show scattering suppression of approximately up to 550 nm of incident light, but a scattering enhancement beyond 550 nm. The magnitude of the scattering suppression is lower, and enhancement is higher by a 550 nm core-shell assembly than the 650 nm and 750 nm core-shell assemblies. A 450 nm core-shell assembly suppresses scattering over a very narrow wavelength range (400 nm - 420 nm) but enhances scattering over a broad visible spectrum (430 nm - 750 nm). This map emphasizes the potential that on-demand



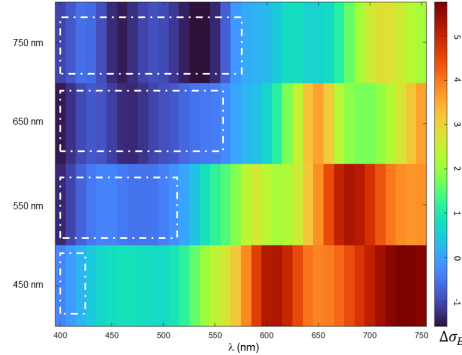


Fig. 3. Comparison of  $\Delta\sigma_E$  ( $\sigma_E^{CS} - \sigma_E^C$ ) for varied core sizes (750 nm, 650nm, 550nm, and 450 nm) coated with 20 nm AuNPs at a filling fraction of 0.30. The Y-axis denotes the core diameters(nm) and X-axis denoting the incident wavelength(nm). The color gradient on the plot surface represents the magnitude of  $\Delta\sigma_E$ . A positive  $\Delta\sigma_E$  refers to scattering enhancement and negative  $\Delta\sigma_E$  is for scattering suppression. The region over which scattering is being suppressed ( $\Delta\sigma_E < 0$ ) is highlighted by a white rectangle (dash-dot-dash) for each core sizes. Region beyond the white rectangle show scattering enhancement ( $\Delta\sigma > 0$ ).

scattering suppression and enhancement for a broad wavelength range can be achieved by varying the diameter of the plasmonic core-shell assembly.

Plasmonic core-shell assemblies achieve total scattering suppression and enhancement by leveraging strong multiple interactions (scattering and absorption) between the plasmonic nanoparticles in the shell and the dielectric core. These interactions significantly alter the spatial and spectral profile of the scattered power. Due to this multiple interactions of the incident light by the AuNPs, we expect an overall decrease in coherence in the scattered field. As a result, the angular side lobes, that are characteristic of diffraction by a bare core, are shifted and suppressed. In other words, we find that differential scattering cross-section ( $\sigma_d$ ) is smoother for the coated cores compared with the bare one, and the smoothing is enhanced as  $\sigma_E$  by an individual AuNP increases. We study the far-field diffraction pattern of these plasmonic assemblies and characterize them in terms of scattering albedo ( $\bar{\omega}_0$ ) and anisotropy ( $g$ ) over the visible spectrum.

Figure 4. Highlights and compares our findings on the  $\sigma_d$  of the 750 nm bare dielectric core (bare, solid black line), same core ( $d = 750$  nm) coated with 5 nm AuNP (5nm, green dash-dotted line) and with 20 nm AuNP (20 nm, red dash line). The 20 nm and 5 nm core-shell structures has a filling fraction  $f = 0.30$ . We compare the far field  $\sigma_d$  of these three structures at two different incident wavelengths where the core-shell structures show suppression and enhancement of scattering at  $\lambda_{inc} = 450$  nm (Fig. 4. A) and  $\lambda_{inc} = 670$  nm (Fig.4.B) respectively. The core-shell structure of the 20 nm AuNP shows minimal back lobe when scattering is suppressed (Fig. 4.A), as well as reduced width and magnitude of the main lobe. Additionally, this structure displays fewer angular side lobes at this wavelength, resulting in a smoother appearance compared to structures with a 5 nm core and no shell. On the contrary, the main lobe of the 5 nm AuNP structure closely follows the main lobe of the bare core while suppressing scattering. The back lobe of the 5 nm AuNP structure is significantly reduced compared to the bare dielectric sphere. Both core-shell structures show an enhancement in scattering at  $\lambda_{inc} = 670$  nm (see Fig. 2A). The core-shell structure of 20nm AuNP generates an enhanced central lobe compared to the 5nm AuNP and bare dielectric core (Fig.4.B). The number of angular sidelobes is also higher than the 5 nm AuNP structure and the bare core, while scattering is enhanced. The main lobe of the

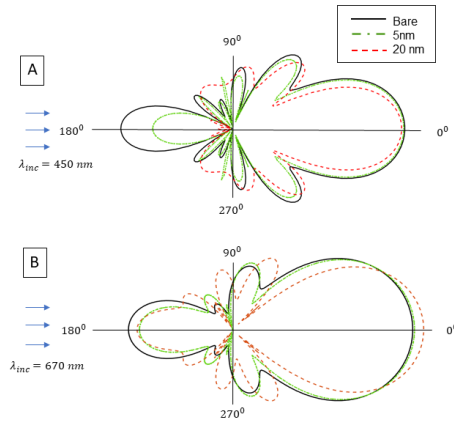


Fig. 4. Polar plot comparing the far-field differential scattering patterns of a 750 nm bare dielectric core and plasmonic core-shell assembly comprised of the same core size but with two types of AuNP shells (5 nm and 20 nm). Incident light is portrayed by three horizontal arrows from left to right. A solid black line denotes the scattering pattern of the bare dielectric sphere (Bare). A green dash-dot line represents the 5 nm AuNP core-shell scattering pattern (5 nm) and a 20 nm core-shell assembly (20 nm) by a red dashed line. Filling fraction is constant for both core-shell types,  $f = 0.30$ . (A). Scattering patterns at 450 nm incident light ( $\lambda_{inc} = 450$  nm). Both 5 nm AuNPs and 20 nm AuNPs shells suppress scattering at this wavelength. (B). Comparing scattering patterns at  $\lambda_{inc} = 670$  nm. Both plasmonic assemblies show scattering enhancement at this wavelength compared with the bare core.

5 nm AuNP closely follows the main lobe of the bare core. The back lobe of both plasmonic structures has almost overlapping magnitude while enhancing scattering (Fig. 4.B). We see that a plasmonic core-shell assembly with a 20 nm AuNP shell can manipulate the spatial and spectral profile of the differential scattering cross section more than an assembly composed of a 5 nm AuNP shell with the same core diameter. Furthermore, these results also suggest that plasmonic core-shell structures emit more power in the forward (along  $0^0$  deg) than backward (along  $180^0$  deg), regardless of whether they suppress or enhance scattering.

We compute the scattering albedo ( $\bar{\omega}_0$ ) of the core-shell assemblies to determine the action of the specific extinction mechanism (scattering and absorption) on the suppression and enhancement of the general scattering.

In Figure 5, we plotted the scattering albedo of the plasmonic metastructures composed of 20 nm AuNP shell ( $f = 0.30$ ) with core sizes varied from 450 nm (green inverted triangle) to 550 nm (blue triangle), 650 nm (red filled circle), and 750 nm (black square). The scattering albedo of the bare dielectric core is shown with a horizontal broken line at  $y = 1$ , as it is barely absorbing over the visible spectrum. Almost all of the incident light is extinguished by the bare dielectric core is due to scattering. Albedo of all the plasmonic core-shell structures falls between 0.7 to 0.8 for shorter incident wavelengths ranging from  $\lambda_{inc} = 400$  to 550 nm. The scattering albedo of the 450 nm plasmonic structure changes somewhat monotonically as we move from shorter to longer wavelengths. Over the range of  $\lambda_{inc} \geq 550$  nm, the albedo increases to a value of  $\bar{\omega}_0 \approx 1$ . For plasmonic structures larger than 450 nm (i.e., 550 nm, 650 nm, and 750 nm), we observe an oscillatory pattern in the albedo for  $\lambda_{inc}$  ranging from 400 nm to 550 nm. The oscillatory pattern for the 550 nm and 650 nm plasmonic structures becomes less pronounced beyond the wavelength of 600 nm, while the 750 nm structures still show noticeable oscillations up to the wavelength of 650 nm. These oscillatory patterns reflect complex strong interactions between

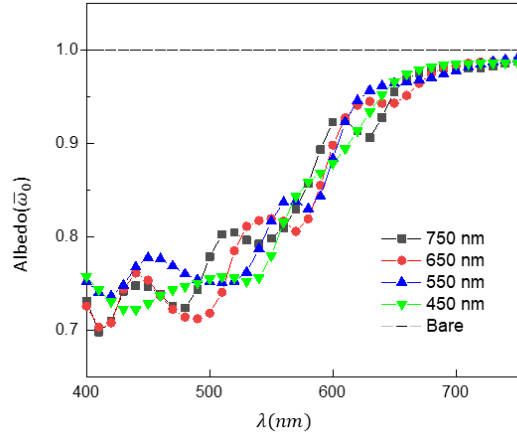


Fig. 5. The scattering albedo ( $\bar{\omega}_0$ ) of plasmonic core-shell structures across the visible wavelength spectrum shown here. The core diameters vary from 450 nm (green inverted triangle) to 550 nm (blue triangle), 650 nm (red filled circle), and 750 nm (black square). The plasmonic shells comprise 20 nm AuNP in all core-shell structures with a constant filling fraction of 0.30. The bare dielectric core has negligible absorption over the visible wavelength range. Consequently, the extinction of the incident light occurs dominantly due to scattering. The albedo of the bare dielectric sphere is indicated by a dashed horizontal line at  $y = 1$ .

the plasmonic shell and the surface of the spherical dielectric core. The 750 nm core has a larger surface area compared to the 450 nm core. As a result, the structure with a 750 nm core can accommodate more gold nanoparticles into its shell at  $f = 0.30$ , leading to a stronger interaction between the shell and the dielectric surface. Over this shorter wavelength range ( $\lambda_{inc} = 450\text{nm}$  to  $\lambda_{inc} = 550\text{nm}$ ), extinction cross-section ( $\sigma_E$ ) of an individual 20 nm AuNP is also higher (See fig 2.B), and it gradually approaches zero beyond 550 nm incident light. Between the 450 nm and 550 nm incident wavelength range, 750 nm, 650 nm, and 550 nm core-shell structures show scattering suppression, while the 450 nm structures show scattering suppression from 400 nm to 420 nm (see Fig.3). These results suggest that approximately 70% of the incident energy is extinct by the core-shell due to scattering, and 30% is due to absorption while suppressing scattering. This is confirming that the main mechanism of this model, which is multiple scattering between the AuNPs and the dielectric core. Scattering suppression of the plasmonic shell depends strongly on scattering and absorption by each individual AuNP. When scattering by an individual metal NP is strong, power incident on the shell of AuNPs undergoes strong multiple scattering in the shell. When absorption by each AuNP is also strong, this strong multiple scattering effectively yields higher absorption of the overall power. Thus, strong scattering creates multiple interactions with strong absorbing AuNPs thereby yielding a suppression in power scattered by the plasmonic shell. The extinction by individual 20 nm AuNP beyond  $\lambda_{inc} = 550\text{ nm}$  exponentially decreases to zero and the scattering is the dominant extinction mechanism over this wavelength range. As a result, beyond 500 nm incident light, scattering albedo increases and approaches unity, referring to all of the incident energy over this wavelength range extinguished due to scattering only, resulting in overall scattering enhancement by these plasmonic metastructures.

We compute the anisotropy ( $g$ ) to identify the amount of power that retains its forward flow after interacting with a bare dielectric core and the corresponding core-shell metal structures. The anisotropy values of the metastructures are obtained by fitting the well-known Heney-

Greenstein(HG) scattering model. According to this model  $\sigma_d$  defined as,

$$\sigma_d^{HG}(\theta) = \frac{\sigma_s}{4\pi} \frac{1 - g^2}{(1 + g^2 - 2g \cos \theta)^{3/2}} \quad (21)$$

Here,  $\sigma_s$  and  $g$  are the only free parameters. HG has been extensively used to study multiple scattering by particles in radiative transfer theory [34]. In fact, it is often used as a simplified model for a dielectric sphere. Because plasmonic core-shell structures have smoother  $\sigma_d$  than the bare core, we find HG is an appropriate model to use here. Figure 6 shows this fit to a 750 nm core-shell structures (black dashed line) with a shell comprising 20 nm AuNP and filling fraction varied from  $f = 0.3$  to  $f = 0.05$ . The differential scattering pattern of the bare dielectric sphere (grey solid line) and the low filling fraction ( $f = 0.05$ ) plasmonic core-shell structures (blue solid line) are comparable in terms of amplitude and phase. However, the higher filling fraction ( $f = 0.30$ ) plasmonic structure shows suppressed angular sidelobes and smoother scattering patterns than the other two structures. We use this fitted value for  $g$  to evaluate the difference in the angular distribution of the scattered power by the metastructures whose core size and AuNP size are varied and compared with the respective bare core.

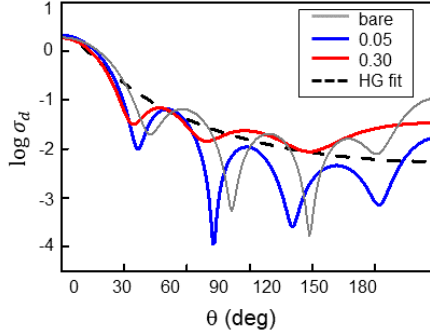


Fig. 6. Comparing the differential scattering cross-section of a 750 nm bare dielectric sphere (shown as a grey solid line) with the same sphere coated with 20 nm AuNP but with varying filling fractions of  $f = 0.05$  (shown as a solid blue line) and  $f = 0.30$  (shown as a solid red line). A Henyey-Greenstein (HG) fit of the higher filling fraction (0.30) structure is represented by a black dashed line.

Figure 7 summarizes our findings on the anisotropy of the bare dielectric core and the corresponding plasmonic metastructures. In Fig. 7. A, we plot anisotropy of a 750 nm bare dielectric sphere (bare, black square), bare core coated with 5 nm AuNP (5nm, green inverted triangle), and bare core coated with 20 nm AuNP (20 nm, red dots) over the visible spectrum. Both core-shell structures have  $f = 0.30$ . A 5 nm AuNP shell has slightly higher anisotropy than the bare core, but a 20 nm AuNP shell can increase the anisotropy significantly. The 5 nm AuNP shell's  $g$  values closely follow the bare cores'. In the case of 20 nm AuNP shells,  $g$  values start near the bare core for shorter wavelengths (400 nm – 500nm) but increase as the wavelength gets longer ( $\lambda_{inc} > 500nm$ ). Beyond 500nm,  $\sigma_E$  of an individual 20 nm AuNP gradually decreases (see Fig 1. B), and the scattering governs total extinction (see Fig 1. C). These results indicate that strong multiple scattering between the 20 nm plasmonic shell and the dielectric core promotes a higher forward directionality of incident power compared to a 5 nm AuNP shell.

In Figure 7B, we compared the anisotropy of various core diameters with the corresponding plasmonic core-shell metastructures across the visible spectrum. The core diameters ranged from

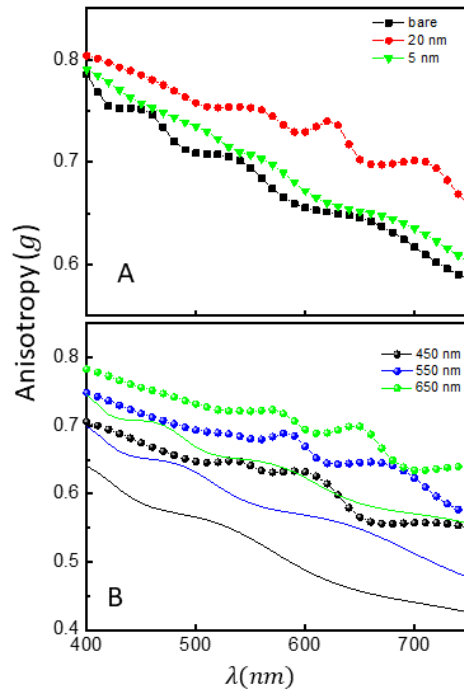


Fig. 7. (A) Comparing anisotropy ( $g$ ) of a 750 nm bare dielectric core (bare, black square) with the plasmonic core-shell structure over the visible spectrum. Plasmonic metastructures are composed of a core of same diameter but coated with 5 nm (5 nm, green triangle) and 20 nm AuNPs (20 nm, red dots) as shell. AuNP filling fractions is 0.30 for both shells. (B) Anisotropy of bare cores with varied diameters are compared with the corresponding plasmonic core-shell structures. Plasmonic shells are comprised of 20 nm AuNP for all core diameters and filling fraction is 0.30. Core diameters are varied from 450 nm (black) to 550 nm (blue), and 650 nm (green). Anisotropy of the bare cores are depicted using a solid lines and the respective core-shells are using dotted lines with same colors.

450 nm (black) to 550 nm (blue) and 650 nm (green). The anisotropy of the core-shell structures is represented using dotted spheres, while the respective bare cores are depicted using solid lines of the same color. The plasmonic shell consists of 20 nm AuNP at  $f = 0.30$  for all core-shell structures. Coating a bare dielectric sphere with randomly distributed 20 nm AuNPs increases the anisotropy of all the core sizes studied here compared to their corresponding cores (Figure 7B). A 450 nm core-shell structure enhances anisotropy more than the 650 nm and 550 nm core-shell assemblies. These results indicate that plasmonic metastructures increase anisotropy for a wide range of core sizes across the visible spectrum. This increase in anisotropy occurs independently of whether a specific core-shell structure suppresses or enhances scattering for a particular incident wavelength. In other words, plasmonic AuNP coating results in a preferential concentration of the scattered power in the forward direction across the visible spectrum.

## 5. Conclusions

Our computational model demonstrates that a coat of randomly distributed AuNPs on a dielectric core can be optimized to modulate the mesoscopic optical properties in the visible spectrum in more than one way. A coating consisting of 20 nm AuNPs with moderate filling fractions

$0.2 < f < 0.3$  results in significant scattering suppression up to  $\lambda = 600$  nm for cores larger than the incident wavelength. But a slight variation of  $f$ , between  $0.1 - 0.2$ , leads to scattering enhancement in the spectral regime  $\lambda > 650$  nm for the same coating. This substantial difference in optical response highlights the versatility of this platform. In addition to this spectral modulation, we observe that the presence of the cover results in a preferential concentration of the scattered power in the forward direction. This reshaping of the angular distribution of power occurs when scattering is suppressed and enhanced. Our results further underscore the critical role of absorption versus scattering by the AuNPs, as we establish that some absorption by the AuNP cover is needed to suppress the scattering of the core. However, scattering is suppressed most when  $f$  is optimal to promote both multiple scattering and absorption with a stronger dependence on former. It is for this reason that 20 nm AuNPs yield more suppression than 5 nm AuNPs. In fact, it is because of multiple scattering in the cover that the angular distribution of scattered power by the coated cores is qualitatively different from that by the bare core. Multiple scattering decreases the overall coherence of scattered light and consequently, suppresses the angular sidelobes in the distribution of scattered power. As a result the forward peak in scattering is more pronounced and the anisotropy factor increases. Through this investigation of the mesoscopic optical properties of nano-assembled plasmonic coatings, we have identified parameter regimes where the cover of AuNPs lead to scattering suppression or enhancement. These results can then guide decisions on tuning AuNP size and filling fraction for a wide range of optical and photonic applications in the visible spectrum, ranging from near-field microscopy to high-resolution imaging.

## Disclosures

The authors declare no conflicts of interest.

## References

1. E. Hutter and J. H. Fendler, "Exploitation of Localized Surface Plasmon Resonance," *Adv. Mater.* **16**, 1685–1706 (2004).
2. K. A. Willets and R. P. Van Duyne, "Localized surface plasmon resonance spectroscopy and sensing," *Annu. Rev. Phys. Chem.* **58**, 267–297 (2007). PMID: 17067281.
3. K. M. Mayer and J. H. Hafner, "Localized Surface Plasmon Resonance Sensors," *Chem. Rev.* **111**, 3828–3857 (2011).
4. J. Zhao, X. Zhang, C. R. Yonzon, *et al.*, "Localized surface plasmon resonance biosensors," *Nanomedicine* **1**, 219–228 (2006). PMID: 17716111.
5. E. Petryayeva and U. J. Krull, "Localized surface plasmon resonance: Nanostructures, bioassays and biosensing—a review," *Anal. Chimica Acta* **706**, 8–24 (2011).
6. A. Alù, "Designer matter: Fascinating interactions of light and sound with metamaterials," *MRS Bull.* **42**, 677–682 (2017).
7. M. B. Ross, C. A. Mirkin, and G. C. Schatz, "Optical Properties of One-, Two-, and Three-Dimensional Arrays of Plasmonic Nanostructures," *The J. Phys. Chem. C* **120**, 816–830 (2016).
8. N. Liu, H. Guo, L. Fu, *et al.*, "Three-dimensional photonic metamaterials at optical frequencies," *Nat. Mater.* **7**, 31–37 (2008).
9. D. García-Lojo, S. Núñez-Sánchez, S. Gómez-Graña, *et al.*, "Plasmonic Supercrystals," *Accounts Chem. Res.* **52**, 1855–1864 (2019).
10. J. Zhu and L. L. Goddard, "All-dielectric concentration of electromagnetic fields at the nanoscale: the role of photonic nanojets," *Nanoscale Adv.* **1**, 4615–4643 (2019).
11. D. McCloskey, J. J. Wang, and J. F. Donegan, "Low divergence photonic nanojets from Si<sub>3</sub>N<sub>4</sub> microdisks," *Opt. Express* **20**, 128–140 (2012).
12. H. Choo, M.-K. Kim, M. Staffaroni, *et al.*, "Nanofocusing in a metal–insulator–metal gap plasmon waveguide with a three-dimensional linear taper," *Nat. Photonics* **6**, 838–844 (2012).
13. R. Gordon, D. Sinton, K. L. Kavanagh, and A. G. Brolo, "A new generation of sensors based on extraordinary optical transmission," *Accounts Chem. Res.* **41**, 1049–1057 (2008).
14. H. Im, H. Shao, Y. I. Park, *et al.*, "Label-free detection and molecular profiling of exosomes with a nano-plasmonic sensor," *Nat. Biotechnol.* **32**, 490–495 (2014).
15. T. W. Ebbesen, H. J. Lezec, H. F. Ghaemi, *et al.*, "Extraordinary optical transmission through sub-wavelength hole arrays," *Nature* **391**, 667–669 (1998).

16. S. Linden, C. Enkrich, G. Dolling, *et al.*, "Photonic Metamaterials: Magnetism at Optical Frequencies," *IEEE J. Sel. Top. Quantum Electron.* **12**, 1097–1105 (2006).
17. S. Mühlig, A. Cunningham, J. Dintinger, *et al.*, "Self-assembled plasmonic metamaterials," *Nanophotonics* **2**, 211–240 (2013).
18. M. Mayer, M. J. Schnepf, T. A. F. König, and A. Fery, "Colloidal self-assembly concepts for plasmonic metasurfaces," *Adv. Opt. Mater.* **7**, 1800564 (2019).
19. S. Ghosh, A. D. Ranjan, S. Das, *et al.*, "Directed Self-Assembly Driven Mesoscale Lithography Using Laser-Induced and Manipulated Microbubbles: Complex Architectures and Diverse Applications," *Nano Lett.* **21**, 10–25 (2021).
20. M. B. Ross, J. C. Ku, V. M. Vaccarella, *et al.*, "Nanoscale form dictates mesoscale function in plasmonic DNA–nanoparticle superlattices," *Nat. Nanotechnol.* **10**, 453–458 (2015).
21. K. L. Young, M. B. Ross, M. G. Blaber, *et al.*, "Using dna to design plasmonic metamaterials with tunable optical properties," *Adv. Mater.* **26**, 653–659 (2014).
22. A. L. Rodarte, R. J. Pandolfi, S. Ghosh, and L. S. Hirst, "Quantum dot/liquid crystal composite materials: self-assembly driven by liquid crystal phase transition templating," *J. Mater. Chem. C* **1**, 5527–5532 (2013).
23. P.-Y. Chen, J. Soric, and A. Alù, "Invisibility and cloaking based on scattering cancellation," *Adv. Mater.* **24**, OP281–OP304 (2012).
24. A. L. Rodarte, B. H. Cao, H. Panesar, *et al.*, "Self-assembled nanoparticle micro-shells templated by liquid crystal sorting," *Soft Matter* **11**, 1701–1707 (2015).
25. M. I. Khan, S. Ghosh, R. Baxter, and A. D. Kim, "Modeling broadband cloaking using 3d nano-assembled plasmonic meta-structures," *Opt. Express* **28**, 22732–22747 (2020).
26. T. C. Choy, *Effective Medium Theory: Principles and Applications* (Oxford University Press, Oxford, 2015), 2nd ed.
27. A. Masłowska, P. Flatau, and G. Stephens, "On the validity of the anomalous diffraction theory to light scattering by cubes," *Opt. Commun.* **107**, 35–40 (1994).
28. C. F. Bohren and D. R. Huffman, *Absorption and scattering of light by small particles* (John Wiley & Sons, 2008).
29. A. Ishimaru, *Wave Propagation and Scattering in Random Media* (Wiley-IEEE, 1997).
30. L. L. Foldy, "The multiple scattering of waves. i. general theory of isotropic scattering by randomly distributed scatterers," *Phys. Rev.* **67**, 107–119 (1945).
31. M. Lax, "Multiple scattering of waves. ii. the effective field in dense systems," *Phys. Rev.* **85**, 621–629 (1952).
32. D. I. Yakubovsky, A. V. Arsenin, Y. V. Stebunov, *et al.*, "Optical constants and structural properties of thin gold films," *Opt. Express* **25**, 25574–25587 (2017).
33. K. Atkinson, "Numerical integration on the sphere," *J. Austral. Math. Soc. Ser. B* **23**, 332–347 (1982).
34. L. G. Henyey and J. L. Greenstein, "Diffuse radiation in the galaxy," *Astrophys. Journal*, vol. 93, p. 70-83 (1941). **93**, 70–83 (1941).